

# Journal of Geophysical Research: Solid Earth

## RESEARCH ARTICLE

10.1002/2015JB011993

### Key Points:

- Deforming oceanic lithosphere behaves as a thin viscous spherical shell
- The power-law relating strain-rate to stress has an exponent of  $\sim 30$  or more
- A trenchward velocity increment of  $5 \text{ mm/a}$  explains earthquake focal mechanisms

### Supporting Information:

- Text S1 and Figure S1
- Data Set S1

### Correspondence to:

R. G. Gordon,  
rgg@rice.edu

### Citation:

Gordon, R. G., and G. A. Houseman (2015), Deformation of Indian Ocean lithosphere: Evidence for a highly nonlinear rheological law, *J. Geophys. Res. Solid Earth*, 120, 4434–4449, doi:10.1002/2015JB011993.

Received 1 MAR 2015

Accepted 15 APR 2015

Accepted article online 25 APR 2015

Published online 10 JUN 2015

## Deformation of Indian Ocean lithosphere: Evidence for a highly nonlinear rheological law

Richard G. Gordon<sup>1</sup> and Gregory A. Houseman<sup>2</sup>

<sup>1</sup>Department of Earth Science, William Marsh Rice University, Houston, Texas, USA, <sup>2</sup>School of Earth and Environment, University of Leeds, Leeds, UK

**Abstract** The width of diffuse oceanic plate boundaries is determined by the rheology of oceanic lithosphere. Here we apply thin viscous sheet models, which have been successfully applied to deformation in several continental deforming zones, to investigate the deformation of oceanic lithosphere in the diffuse oceanic plate boundaries between the India, Capricorn, and Australia Plates. We apply kinematic boundary conditions based on the current motion between these plates. We neglect buoyancy forces due to plate thinning or thickening and assume that the thin viscous sheet has the same depth-integrated nonlinear viscosity coefficient everywhere. Our initial models have only one adjustable parameter,  $n$ , the power-law exponent, with  $n = 1, 3, 10, 30$ , and  $100$ . The predicted width of the deforming zone decreases with increasing  $n$ , with  $n \geq 30$  explaining the observations. This  $n$  value is higher than has been estimated for continental lithosphere and suggests that more of the strength of oceanic lithosphere lies in layers deforming by faulting or by dislocation glide than for continental lithosphere. To obtain a stress field that better fits the distribution and type of earthquake focal mechanisms in the diffuse oceanic plate boundary, we add a second adjustable parameter, representing the effect of slab pull stretching the oceanic plate near the Sumatra Trench. We show that an average velocity increment on this boundary segment of  $5 \text{ mm a}^{-1}$  (relative to the average velocity of the India and Australia Plates) fits the observed distribution of fault types better than velocities of  $3.3 \text{ mm a}^{-1}$  or  $10 \text{ mm a}^{-1}$ .

## 1. Introduction

Plate tectonics has transformed our view of how our planet works. Two central tenets of plate tectonics in its original form were that the plates are rigid and that the boundaries are narrow. In the early days of plate tectonics it was recognized that plate boundaries through continents were typically diffuse [e.g., Atwater, 1970; Tapponnier and Molnar, 1977], but it was still believed that oceanic plate boundaries were generally narrow despite some anomalies [e.g., Isacks et al., 1968; Curray and Moore, 1971; Eittreim and Ewing, 1972; Weissel et al., 1980]. Eventually, however, diffuse plate boundaries were recognized in many places in the ocean basins [e.g., Ball and Harrison, 1970; Stein and Okal, 1978; Minster and Jordan, 1978; Wiens et al., 1985; Gordon et al., 1990; DeMets et al., 1990, 2010; Bull, 1990; Bull and Scrutton, 1990; Gordon and Stein, 1992; Chamot-Rooke et al., 1993; Jestin et al., 1994; Royer and Gordon, 1997, 1998; Chu and Gordon, 1999; Cande and Stock, 2004]. While the strain-rates in diffuse oceanic plate boundaries are typically lower than in diffuse continental boundaries, about the same fraction of diffuse boundary is located in oceanic lithosphere as in continental lithosphere. Accepting the concept of diffuse plate boundaries helps to preserve the rigid plate approximation for the  $\approx 85\%$  of the lithosphere outside of diffuse plate boundaries [Gordon and Stein, 1992].

While processes at narrow oceanic plate boundaries have been intensively investigated for decades, those in diffuse oceanic plate boundaries have been studied much less. Many fundamental questions remain unanswered or poorly constrained. For example, what controls the length scale of this deformation? What are the relative contributions of the different deformation mechanisms that are active in deforming oceanic lithosphere? Why do diffuse oceanic plate boundaries occur where they do and not elsewhere? What controls the sense and style of deformation (i.e., normal faulting versus strike-slip faulting versus thrust faulting)?

Diffuse plate boundaries in oceanic lithosphere occur in many places. Displacement rates range up to  $\approx 15 \text{ mm a}^{-1}$  and strain-rates up to  $\sim 10^{-16} \text{ s}^{-1}$  [Gordon, 2000]. Diffuse oceanic plate boundaries are much wider than traditionally defined narrow plate boundaries such as mid-ocean ridges for which the main

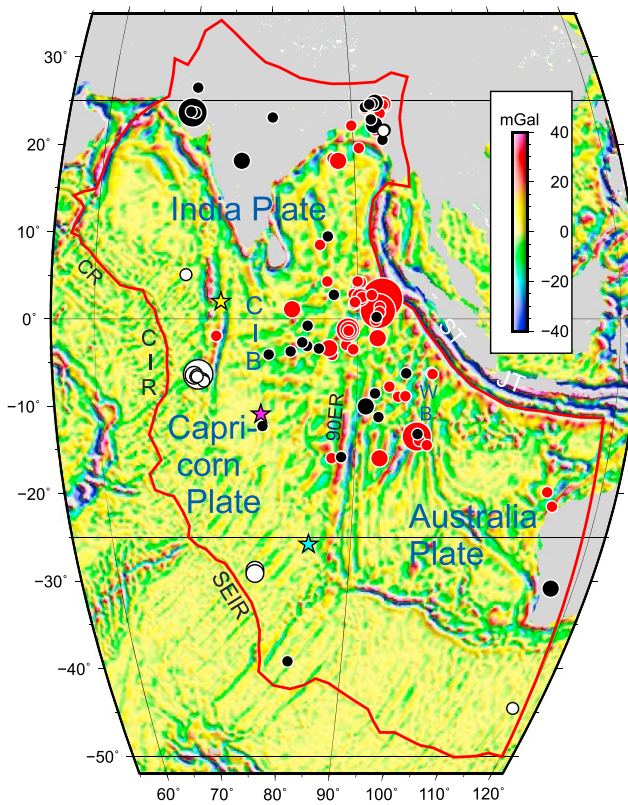


**Figure 1.** Gravity and seismicity of part of the Indo-Australia composite plate: Earthquake epicenters  $>2^\circ$  distant from the narrow plate boundaries are shown for events with moment between  $10^{17}$  and  $10^{22}$  N m ( $5.3 < M_w < 8.6$ ) from 1976 to 2014. Symbol size increases with magnitude, and color indicates mechanism, based on which of the principal axes of the moment tensor is nearest to vertical: white for normal, red for strike slip, and black for thrust. Further details of the earthquake data obtained from the Global centroid moment tensor project [www.globalcmt.org] are provided in the Appendix. Background map shows a band pass-filtered (100 to 400 km wavelength) version of the gravity grid of Sandwell *et al.* [2014]. The solid red line shows the boundary of the computational domain used in our calculations, corresponding to the plate boundary except where it cuts across Australia. The three stars represent the poles of relative plate rotation India-Capricorn (yellow), India-Australia (magenta), and Capricorn-Australia (blue) from MORVEL [DeMets *et al.*, 2010]. Abbreviations: CIB, Central Indian Basin; 90ER, Ninetyeast Ridge; WB, Wharton Basin; ST, Sumatra Trench; JT, Java Trench; CR, Carlsberg Ridge; CIR, Central Indian Ridge; and SEIR, Southeast Indian Ridge.

which assume 2-D plane strain (in vertical slices) to elucidate the interaction of folding and faulting in a contractional deformation [Zuber and Parmentier, 1996; Montesi and Zuber, 2003; Gerbault *et al.*, 1999; Gerbault, 2000; Delescluse *et al.*, 2008]. Unlike the 2-D vertical plane models, which allow an explicit vertical stratification of properties, the thin viscous sheet models can be used to investigate lateral variations in style of deformation and stress including variations in the orientation of principal stresses and the magnitudes of the strain-rates. Our models further complement prior studies of elastic shells, which have been successful at reproducing the observed pattern of the orientation of intraplate stress and have enabled limits to be determined on the relative sizes of tractions acting on the plate [e.g., Cloetingh and Wortel, 1985; Coblenz *et al.*, 1998; Sandiford *et al.*, 2005]. As Indo-Australia lithosphere deforms by faulting at many places [e.g., Chamot-Rooke *et al.*, 1993], however, an elastic model falls short in describing the deformation and rheology of these regions.

boundary zone is 1 to 2 km wide. In contrast, the diffuse boundary between the India and Australia Plates seaward of the Java-Sumatra Trench is thousands of kilometers wide (Figure 1). The inferred strain-rates are 1 to 3 orders of magnitude greater than the average oceanic intraplate strain-rate inferred from seismic moment release or thermal contraction in old oceanic lithosphere but many orders of magnitude lower than in traditional narrow plate boundaries [Gordon, 2000; Kumar and Gordon, 2009].

Herein, we build on the most recent investigation of global plate motions, which includes improved kinematic boundary conditions for the diffuse boundary between the India, Capricorn, and Australia Plates [DeMets *et al.*, 2010]. We use observations of the deformation to quantify the rheology of the lithosphere and the variation of the stress field in this region through the application and analysis of thin viscous sheet models. Using data from earthquake seismology and marine geophysics, we constrain the vertically integrated rheology of oceanic lithosphere, which can be interpreted in terms of the relative contributions of lithospheric deformation mechanisms that include faulting, fracturing, dislocation glide, and dislocation creep.

Our investigation complements and builds on prior kinematic studies of oceanic lithospheric deformation [Tinnon *et al.*, 1995; Kreemer *et al.*, 2003; Burbidge, 2004; Delescluse and Chamot-Rooke, 2007]. Our results also complement those obtained from dynamical models of oceanic lithospheric deformation

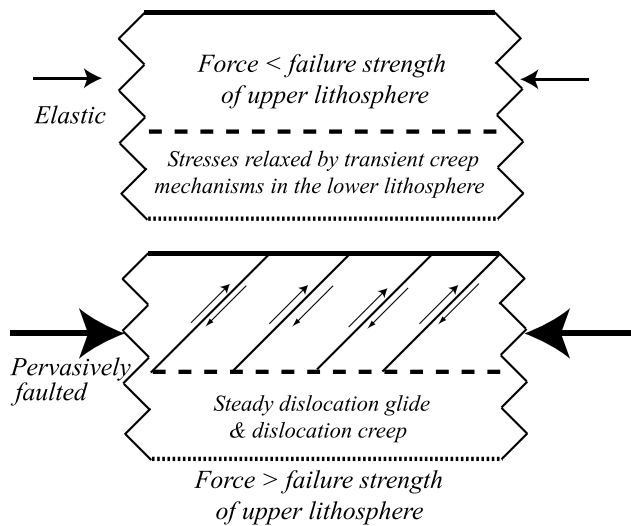


**Figure 2.** Deformation of oceanic lithosphere. (top) When the lithosphere is loaded at a force per unit length less than the failure strength of the upper lithosphere, the load is supported by elastic deformation. Creep of the lower lithosphere progressively concentrates load in the upper lithosphere. Dislocation glide obeys an exponential law, and dislocation creep obeys a power-law for which strain rate is proportional to shear stress raised to the  $n$ th power, with  $n$  typically having a value of  $\approx 3$  [Kohlstedt *et al.*, 1995]. (bottom) When the lithosphere is loaded at a force per unit length exceeding the failure strength of the upper lithosphere, the upper lithosphere fails pervasively and the lower lithosphere must support the excess load through steady state deformation. The lithosphere as a whole, that is, as described by its vertically integrated rheology, is well approximated by a power-law fluid [Sonder and England, 1986]. Schematic faults are shown dipping uniformly, but real oceanic deforming zones have faults of variable dip and polarity.

A model of a thin sheet of power-law fluid, which has been used before to successfully represent lithospheric deformation in the continents, may be equally useful for estimating the vertically averaged properties of deforming oceanic lithosphere. For example, Zatman *et al.* [2001, 2005] used simple analytical and numerical models of a thin viscous sheet to explore the relation between the pole of relative motion of component plates bounding a diffuse oceanic plate boundary and the orientation of the torque that each component plate exerts on the other. They found that for a power-law exponent  $n \geq \approx 3$ , the dependence of the torque orientation on the rotation orientation was insensitive to the value of  $n$ .

Earlier investigations of the thin-sheet model applied to continental regions found power-law exponents in the range  $\approx 3$  to 10 [e.g., England and Houseman, 1986; England and Molnar, 1991, 1997; Neil and Houseman, 1997]. More recently, however, Dayem *et al.* [2009] found that the vertically integrated rheology of the lithosphere beneath the Altyn Tagh Fault zone on the Tibetan Plateau may be better described with a power-law exponent even greater than 10. An inferred value of  $\approx 3$  suggests that most of the strength in deforming continental lithosphere lies in the part of the lithospheric mantle that deforms by creeping flow [Sonder and England, 1986]. Because oceanic lithosphere has a much thinner crust and the mantle is generally more resistant to creeping flow, fracturing and faulting typically extend to greater depth in oceanic lithosphere and the relevant exponent may then be greater than 3. The vertically integrated constitutive law for the lithosphere combines the properties of the upper lithosphere, which deforms by faulting and fracturing and for which the appropriate power-law exponent is  $n \rightarrow \infty$ , and the lower lithosphere, which deforms by dislocation glide [Goetze, 1978; Evans and Goetze, 1979; Raterson *et al.*, 2004; Dayem *et al.*, 2009; Mei *et al.*, 2010] and obeys an exponential law, and by dislocation creep, which obeys a power-law with  $n \approx 3$  [Kohlstedt *et al.*, 1995]. Although only the lowest layer obeys a power-law, the integrated behavior of deforming lithosphere can be well approximated by a power-law [Sonder and England, 1986].

We assume that the vertically averaged rheology of deforming oceanic lithosphere can be modeled as a thin viscous sheet of fluid obeying a power-law constitutive relation [cf. Bird and Piper, 1980; England and McKenzie, 1982; Sonder and England, 1986; Viloteau *et al.*, 1982]. When loaded by in-plane compression at less than the elastic limit, the upper oceanic lithosphere deforms elastically with the lower lithosphere deforming by solid-state creep as the stresses relax [Kusznir and Bott, 1977] (Figure 2, top). When the lithosphere is loaded beyond the failure strength of the upper elastic layer, that layer fails by pervasive faulting [cf. Gerbault *et al.*, 1999]. With part of the load supported by solid-state flow of the lower lithosphere and part supported by sliding on faults of the upper lithosphere (Figure 2, bottom), the effective constitutive law of the depth-averaged structure may be highly nonlinear. The steady rate of motion between the India and Capricorn Plates for the past 8 Ma is suggestive of a fluid-like response of the deforming oceanic lithosphere in their mutual diffuse oceanic plate boundary [DeMets *et al.*, 2005].

A key goal of the present work is to investigate sensitivity of the distribution of the deformation to the value of  $n$ , and thus whether the distribution of the deformation might place constraints on the vertically integrated rheology of oceanic lithosphere.

## 2. Methods

To solve for the deformation field of a thin viscous spherical shell, we adapt the Cartesian thin viscous sheet formulation previously applied to geodynamical problems [e.g., *Bird and Piper, 1980; England and McKenzie, 1982; Houseman and England, 1986, 1993*]. In this formulation the lithosphere is represented as a thin layer which deforms coherently. The body forces acting in the horizontal directions are zero, so the horizontal components of the divergence of the deviatoric stress tensor are equal to minus the gradient of the pressure, and the pressure is determined by the radial stress. The stresses are averaged over a layer of nominal thickness  $L \approx 100$  km, the base of which is an equipotential surface. This layer is assumed to include all of the load-bearing parts of the lithospheric plate and, where the lithosphere is thin, some thickness of asthenosphere. Within this layer the angular velocities describing horizontal displacements are assumed invariant with depth. In spherical coordinates, the variation of the depth-averaged deviatoric stress components  $\bar{\tau}_{ij}$  is then described by

$$\frac{2}{r} \frac{\partial \bar{\tau}_{\theta\theta}}{\partial \theta} + \frac{1}{r} \frac{\partial \bar{\tau}_{\varphi\varphi}}{\partial \theta} + \frac{1}{r \sin \theta} \frac{\partial \bar{\tau}_{\theta\varphi}}{\partial \varphi} + \frac{\cot \theta}{r} (\bar{\tau}_{\theta\theta} - \bar{\tau}_{\varphi\varphi}) = -\frac{1}{r} \frac{\partial \bar{\sigma}_{rr}}{\partial \theta} \quad (1)$$

$$\frac{1}{r} \frac{\partial \bar{\tau}_{\theta\varphi}}{\partial \theta} + \frac{1}{r \sin \theta} \frac{\partial \bar{\tau}_{\theta\theta}}{\partial \varphi} + \frac{2}{r \sin \theta} \frac{\partial \bar{\tau}_{\varphi\varphi}}{\partial \varphi} + 2 \frac{\cot \theta}{r} \bar{\tau}_{\theta\varphi} = -\frac{1}{r \sin \theta} \frac{\partial \bar{\sigma}_{rr}}{\partial \varphi} \quad (2)$$

where  $\theta$  and  $\varphi$  are the colatitude and longitude (in radians), respectively,  $r$  is the radial coordinate, and  $\bar{\sigma}_{rr}$  is the depth-averaged radial (vertical) stress component, which can be directly related to the gravitational potential energy of the lithospheric column [*Le Pichon, 1983*]. We assume here a simplified non-Newtonian viscous constitutive law in which deviatoric stress is related to strain-rate  $\dot{\varepsilon}_{ij}$  by

$$\bar{\tau}_{ij} = B \dot{E}^{(1-n)/n} \dot{\varepsilon}_{ij} \quad (3)$$

where  $\dot{E} = \sqrt{\dot{\varepsilon}_{ij} \dot{\varepsilon}_{ij}}$  is the second invariant of the strain-rate tensor,  $n$  is the stress exponent, and  $B$  is a material constant which represents a depth-averaged viscosity coefficient. We assume in this initial study that the index  $n$  and the coefficient  $B$  do not vary with position across the domain of the solution, which represents the northwestern part of the Indo-Australia composite plate (Figures 1 and 3).

The horizontal strain-rates are related to the horizontal velocity components by

$$\dot{\varepsilon}_{\theta\theta} = \frac{1}{r} \frac{\partial u_\theta}{\partial \theta}; \quad \dot{\varepsilon}_{\varphi\varphi} = \frac{1}{r \sin \theta} \frac{\partial u_\varphi}{\partial \varphi} + \frac{u_\theta}{r} \cot \theta; \quad \dot{\varepsilon}_{\theta\varphi} = \frac{1}{2} \left( \frac{1}{r \sin \theta} \frac{\partial u_\theta}{\partial \varphi} + \frac{1}{r} \frac{\partial u_\varphi}{\partial \theta} - \frac{u_\varphi}{r} \cot \theta \right) \quad (4)$$

The system of equations (1)–(4) is solved for  $u_\varphi, u_\theta$  subject to a set of prescribed displacement rates on the external periphery of the spherical sheet, using the finite element method. When we consider the dimensionless form of equations (1) and (2), we find that the gradients of radial stress on the right-hand side may be neglected if the viscosity of the plate is sufficiently great. Using the terminology introduced by *England and McKenzie [1982]*, the Argand number and hence the terms on the right-hand side of (1) and (2) are here assumed to be zero. Normal horizontal stress components  $\sigma_{aa}$  obtained from these solutions are relative to the average vertical stress of a reference column (unconstrained under this assumption) and are related to their deviatoric components by

$$\sigma_{aa} = \tau_{aa} - \tau_{rr} \quad (5)$$

The digital plate boundary assumed here (Figure 1) is obtained from *Bird [2003]*, but the plate is arbitrarily truncated by a nearly meridional boundary between longitudes 119°E and 120°E (Figure 3). East of this line, deformation of the plate is not relevant to the question of how oceanic lithosphere between the India, Capricorn, and Australia Plates is deforming; omitting this part of the plate enables us to obtain better resolved solutions. A finite element mesh of approximately equidimensional triangles is generated in the solution domain using the triangle program of *Shewchuk [2002]*. The size of the triangular elements was varied as necessary to obtain well-resolved solutions. We used meshes with 45,818 elements routinely and 91,888 elements to check resolution.

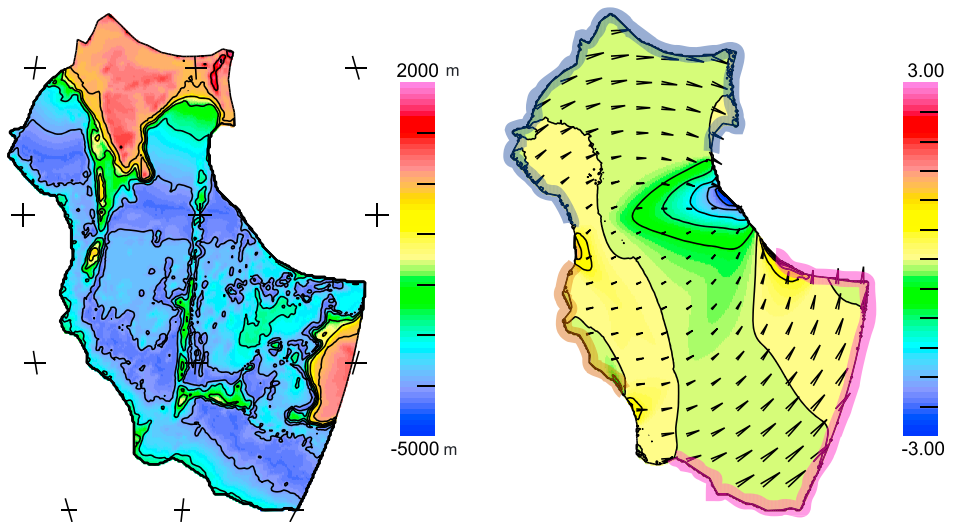


**Figure 3.** Domain of the spherical sheet finite element calculations, showing (left) smoothed topography and bathymetry from the ETOPO5 data set (for geographical orientation, with coordinate marks shown at intervals of 30° in longitude and 25° in latitude) and (right) velocity field (arrows) and N-S strain rate (color) for  $n = 30$ . Angular velocities are applied to the colored boundary segments as defined in Table 1. On the uncolored boundary segments, diffuse deformation occurs as the angular velocity is smoothly tapered from one plate-like segment to the next. The longest arrow on the diagram has a dimensional velocity of 15.5 mm a<sup>-1</sup> in a reference frame in which the India and Australia Plates have equal and opposite angular velocity. N-S strain rate is labeled in dimensionless units; a dimensionless strain rate of 3 corresponds to 0.93% Ma<sup>-1</sup> ( $3 \times 10^{-16}$  s<sup>-1</sup>); positive strain rate is extensional, and strain-rate changes sign on the green/yellow contour.

The finite element method was adapted from the Cartesian method described by *Houseman and England* [1986] by projecting the spherical problem onto the Cartesian plane using the sinusoidal equal area projection. Choosing the unit length in this problem to be  $R$ , the radius of the spherical surface, and  $\varphi_0$  the central longitude of the projection, it is convenient to use the dimensionless coordinate system:

$$y = \theta; \quad x = (\varphi - \varphi_0)\sin\theta \quad (6)$$

with the angular coordinates expressed in radians. In these calculations we choose  $\varphi_0 = 81.5^\circ\text{E}$  to simplify comparison of model predictions with data available on that meridional profile. With this method, the equations (1)–(4) can be represented in a discretized form which is similar to that used in the Cartesian problem and is readily implemented in the two-dimensional viscous flow program *basil* [*Houseman et al.*, 2008]. The vertical strain-rate can then be evaluated as

$$\dot{\epsilon}_{rr} = -\dot{\epsilon}_{\theta\theta} - \dot{\epsilon}_{\varphi\varphi} = -\frac{\partial u_\varphi}{\partial x} - \frac{\partial v_\theta}{\partial y} - v_\theta \cot\theta \quad (7)$$

and other quantities that characterize the strain-rate and stress fields can similarly be obtained.

In principle the problem defined here can be completed by specifying either displacement rate or traction conditions on the periphery of the domain. In this study we choose to specify displacement rate conditions based on the known relative displacement of the three major elements of the Indo-Australia composite plate (India, Australia, and Capricorn) [*Royer and Gordon*, 1997; *Gordon et al.*, 2008; *DeMets et al.*, 2010]. We define three domain boundary segments (Figure 3 (right) and Table 1) which partially delimit these three plate segments. If the plate is rigidly attached to the relevant plate boundary segment, then we may impose the observed angular velocity vector  $\omega$  of that plate by setting the velocities on the plate boundary segment using

$$\mathbf{u} = \boldsymbol{\omega} \times \mathbf{R} \quad (8)$$

If the plate is rigid, it must move with the angular velocity prescribed on its boundary. A boundary segment with a distinct angular velocity causes the regions that are partially enclosed by that segment to have low rates of deformation; these approximately rigid regions are separated by zones of deformation. Between plate boundary segments with endpoints specified in Table 1, we define a gradual transition from one

**Table 1.** Velocities Applied to Boundary Segments Are Calculated Using the Angular Velocities (Rate  $\omega$  in  $^{\circ}$  Ma $^{-1}$ , Pole Longitude  $\varphi$ , and Latitude  $\theta$ ) of the Three Parts of the Indo-Australian Composite Plate From the MORVEL Angular Velocities [DeMets *et al.*, 2010]<sup>a</sup>

	$\omega$	$\varphi$	$\theta$	$\varphi_{b1}$	$\theta_{b1}$	$\varphi_{b2}$	$\theta_{b2}$
Australia	0.178	78.9	-10.9	78.2	-35.7	109.6	-10.4
India	-0.178	78.9	-10.9	91.6	10.0	67.9	-1.9
Capricorn	0.096	43.8	56.3	68	-9	74	-28
Sumatran edge segment	0.059, 0.089, and 0.178	8.2	52.2	97.1	0.0		

<sup>a</sup>A constant angular velocity is added to each plate vector to obtain a reference frame in which the Australia-Capricorn and India-Capricorn angular velocities are equal and opposite. The relevant velocity is applied to all points on the boundary segment between  $(\varphi_{b1}, \theta_{b1})$  and  $(\varphi_{b2}, \theta_{b2})$ . Between segments the velocity is calculated using a linear interpolation of the two angular velocities either side. The Sumatran edge segment angular velocity defines the velocity applied to points along the plate boundary near Sumatra; here three different peak values (Figure 7) are applied at the point  $(\varphi_{b1}, \theta_{b1})$  linearly tapered to the endpoint of the adjoining Indian or Australian plate boundary segment.

angular velocity vector to another, using a cosine<sup>2</sup> taper function which changes the vector smoothly from the end of one boundary segment to the beginning of the next. We choose to present the solutions in the reference frame in which the Australia and India angular velocities are equal and opposite; strain-rate fields are invariant to the choice of reference frame. To recognize the influence of in-plane stress produced by the oceanic lithosphere subducted beneath Sumatra, in some solutions we separately set a component of approximately trench-normal velocity linearly tapered to a maximum on the domain boundary segment near Sumatra. We consider that the amplitude of this vector (applied to the Sumatran boundary segment) is a free variable, which we adjust to improve the model predictions. The angular velocities used in these calculations are summarized in Table 1.

In discussing the results of these calculations, we quantify the faulting style that we expect to see on a surficial brittle layer, which deforms coherently with the primarily viscous lithospheric sheet. We decompose the diagonalized strain-rate tensor at any point in the solution domain into a pair of double couples, following the method of Houseman and England [1986]. The decomposition of a triaxial strain-rate field into a pair of double couples is not unique, but we resolve the ambiguity by choosing the pair of double couples for which the rate of work is least. For principal horizontal strain-rates  $\dot{\varepsilon}_1$  and  $\dot{\varepsilon}_2$ , where  $\dot{\varepsilon}_1 \geq \dot{\varepsilon}_2$ , the ratio  $\dot{\varepsilon}_2/\dot{\varepsilon}_1$  defines a smoothly varying function which specifies the relative amplitude of each type of faulting needed to accommodate the local strain-rate field. We contour the quantity

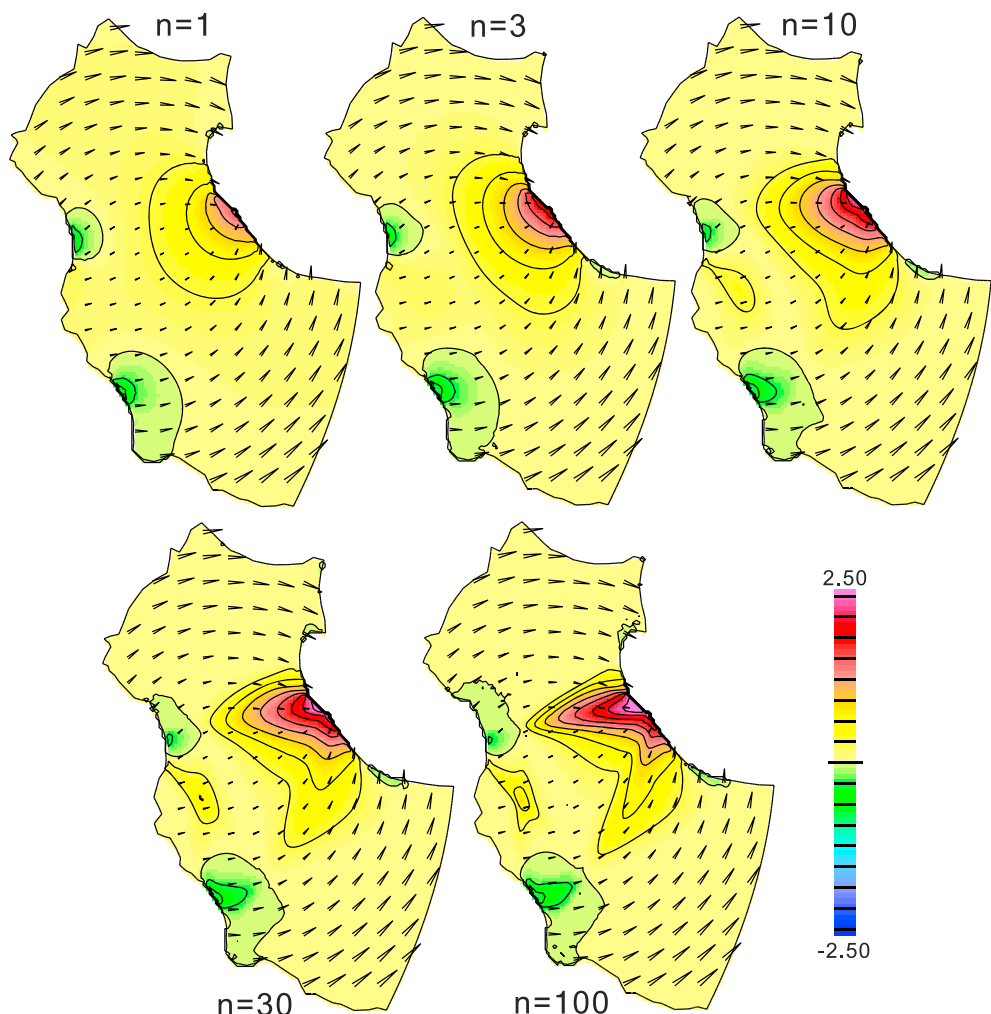
$$p = \left( \frac{3}{4} + \frac{1}{\pi} \tan^{-1} \left( \frac{\dot{\varepsilon}_2}{\dot{\varepsilon}_1} \right) \right) \quad (9)$$

whose value (between 0 and 1) indicates the expected style of surficial faulting as follows: thrust only ( $\dot{\varepsilon}_1 \leq 0$  and  $\dot{\varepsilon}_2 \leq 0$ ;  $0 \leq p \leq 0.25$ ), thrust + strike slip ( $\dot{\varepsilon}_1 + \dot{\varepsilon}_2 \leq 0$  and  $\dot{\varepsilon}_1 \dot{\varepsilon}_2 \leq 0$ ;  $0.25 < p < 0.5$ ), strike slip only ( $\dot{\varepsilon}_1 + \dot{\varepsilon}_2 = 0$  and  $\dot{\varepsilon}_1 \dot{\varepsilon}_2 < 0$ ;  $p = 0.5$ ), normal + strike slip ( $\dot{\varepsilon}_1 + \dot{\varepsilon}_2 \geq 0$  and  $\dot{\varepsilon}_1 \dot{\varepsilon}_2 \leq 0$ ;  $0.5 < p < 0.75$ ), or normal only ( $\dot{\varepsilon}_1 \geq 0$  and  $\dot{\varepsilon}_2 \geq 0$ ;  $0.75 \leq p \leq 1$ ).

Contour plots of the quantity  $p$  can thus be interpreted as showing the relative magnitudes of dip-slip and strike-slip deformation; strike slip exceeds dip slip in the range  $0.375 < p < 0.625$ .

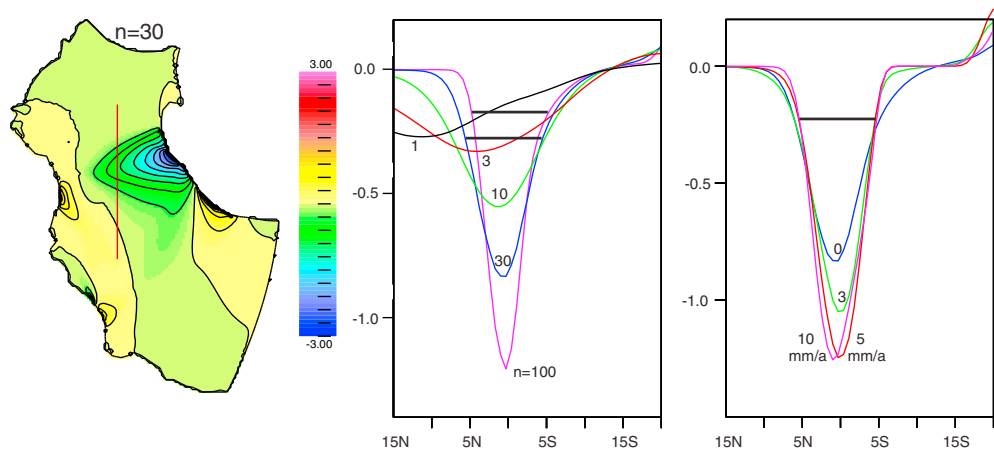
### 3. Results

Figure 4 shows the distributions of plate velocity and thickening rate  $\dot{\varepsilon}_{rr}$  for  $n = 1, 3, 10, 30$ , and  $100$ . There is a clear qualitative progression in the character of the deformation as  $n$  increases. For  $n = 1$ , strain-rates are greatest near the boundary segments along which the imposed angular velocity varies, and they decrease with distance from the boundary segment. The zone of significant strain-rates reaches out into the adjoining plate segments. With increasing  $n$  the north-south extent of the deformation zone decreases and two ridges of high strain-rate develop, connecting the high strain-rate zones on the eastern and western sides of the external boundary. The three-component plates become more plate like and the boundaries between them more clearly defined with increasing  $n$  as the strain-rate gradient steepens in these deformation zones. For  $n \geq 30$  the crests of the ridges of high strain-rate define the domain boundaries between the India, Capricorn, and Australia Plates. The increased density of contours defining these ridges shows the decreasing width of the domain boundary as  $n$  is increased to 100.



**Figure 4.** Contour map of dimensionless vertical strain rate in the Indo-Australian composite plate for  $n = 1, 3, 10, 30$ , and  $100$ . Positive values indicate that the lithosphere is thickening, whereas negative values indicate that the lithosphere is being thinned. The angular velocity vectors of the three-component plates specified in Table 1 are used to impose boundary velocities on the boundary segments shown in Figure 3. Arrows show the velocities of interior points in the solution. Refer to Figure 3 for scaling of velocity arrows and strain rate.

The strongest constraint on the north-south extent of deformation in the India-Capricorn diffuse plate boundary comes from a seismic profile in the Central Indian Basin along  $81.5^{\circ}\text{E}$  from the coast of Sri Lanka to  $14^{\circ}\text{S}$  [Chamot-Rooke *et al.*, 1993], which indicates that deformation is concentrated between the equator and  $8^{\circ}\text{S}$ . The location of the northern edge of this zone is constrained because few faults can be inferred on seismic images north of the equator. The sediment thickness is negligible south of  $8^{\circ}\text{S}$ , however, and faults may exist there that were not imaged. Images of satellite gravity (Figure 1) suggest that lithospheric folds, and hence deformation, continue to  $\approx 10^{\circ}\text{S}$ . Minor deformation may continue farther south. In any event, however, it appears that perhaps 80% or more of the deformation is confined to a zone of width  $10^{\circ}$ , as indicated by the horizontal bar in Figure 5. For comparison with these observations, we show in Figure 5 the corresponding model profile of north-south longitudinal strain-rate as a function of latitude along  $81.5^{\circ}\text{E}$  from  $17.5^{\circ}\text{S}$  to  $15^{\circ}\text{N}$  for values of  $n$  between 1 and 100. The model profiles show the north-south extent of deformation decreasing with increasing  $n$ ; of the five model profiles, only those with  $n \geq 30$  have most of the current deformation rate confined to a zone of width  $10^{\circ}$ . The fraction of deformation within the zone of length  $10^{\circ}$  is estimated as the ratio of two integrals (of strain-rate): the first limited by the  $10^{\circ}$  long segment and the second to include all of the nonzero strain-rates described by the model curve.



**Figure 5.** (left) Map of dimensionless north-south strain rate  $\dot{\epsilon}_{\theta\theta}$  for  $n=30$  and (middle and right) locations of profiles. Model profiles of the zonal (north-south) strain rate  $\dot{\epsilon}_{\theta\theta}$  as a function of latitude along 81.5°E in the Indo-Australian composite plate for  $n = 1, 3, 10, 30$ , and 100 (1 dimensionless unit corresponds closely to  $10^{-16} \text{ s}^{-1}$  or  $0.31 \text{ Ma}^{-1}$ ) are shown in Figure 5 (middle). Shown for comparison is a bar of length  $10^\circ$  representing the observed north-south width of the zone of thrust faulting affecting this part of the Indian Ocean. The same profiles for  $n = 30$  with additional average imposed flux along the Sumatra Trench, 0, 3.3, 5, and  $10 \text{ mm a}^{-1}$ , are shown in Figure 5 (right).

In the  $n = 30$  and  $n = 100$  cases, deformation in the Central Indian Basin is maximum near the equator (1 to  $2^\circ\text{N}$ ), in reasonable agreement with the observed pattern of deformation. The locus of deformation in the model is strongly influenced by the assumed latitude of the India-Capricorn pole of rotation of  $2^\circ\text{N}$  and by the longitudinal width of the plate, which is narrowest between the equator and  $10^\circ\text{N}$ . The latitudinal extent ( $10^\circ\text{N}$  to  $10.4^\circ\text{S}$ , Table 1) of the diffuse contractional boundary condition that we assume along the Sumatran Trench also may play a minor role in the localization of strain, but as Figure 4 shows, the principal factor that causes strain localization is the nonlinearity of the constitutive law.

In Figure 6 we examine the style of faulting predicted for the viscous deformation fields, using contour plots of the parameter  $p$  defined by equation (9). The results for  $n = 100$  resemble those for  $n = 10$  for both distribution of the orientation of principal stresses and the predicted values of the parameter  $p$ . Thus, while the distribution of strain-rates is sensitive to the value of the power-law exponent,  $n$ , the orientations of principal stresses are not. The standout feature in these plots is a line which connects the two poles of rotation (India-Capricorn and Australia-Capricorn), to the east of which deformation is dominated by horizontal contraction, whereas to the west horizontal extension occurs in localized regions either side of the Capricorn Plate. This line is analogous to the neutral surface familiar from studies of elastic plate flexure and is also seen in other situations where a bending moment is applied to a viscous slab [e.g., *Roberts and Houseman, 2001*]. The greatest compressive stress changes from near north-south to the east of this line to near east-west on the western side. Just to the eastern side of this line, a zone of contraction produced by thrust faulting with both NNW and ENE  $P$  axes is predicted in the Central Indian Ocean Basin, but straining in most of the composite plate occurs by a combination of thrust and strike-slip faulting, both with  $P$  axes between NW and NNW. In these models thrust faulting is predicted to exceed strike-slip faulting, except in a small region adjacent to the Sumatran boundary segment and near the Central and Southeast Indian Ridges (Figure 6). The model, however, would be in better agreement with the observed focal mechanisms (Figure 1) if it predicted a higher proportion of strike-slip mechanisms across the contractional eastern part of the domain of diffuse plate deformation.

We recognize, however, that the boundary conditions we have applied in these experiments probably do not adequately represent the effect of a downdip force produced by the plate subducting beneath Sumatra [Sandiford *et al.*, 2005]. We add this force into the model in an approximate way by specifying an outward directed boundary-normal velocity distribution along the Sumatran edge between the Australia and India component plates. This additional angular velocity is defined by pole coordinates (Table 1) chosen to be approximately  $90^\circ$  distant along strike from the midpoint of this boundary segment at  $2^\circ\text{N}$ ,  $95^\circ\text{E}$  and an amplitude that we treat as unknown. The imposed velocity is tapered linearly to the India pole on one side and to the Australia pole on the other side of its peak value. We emphasize that this condition does not

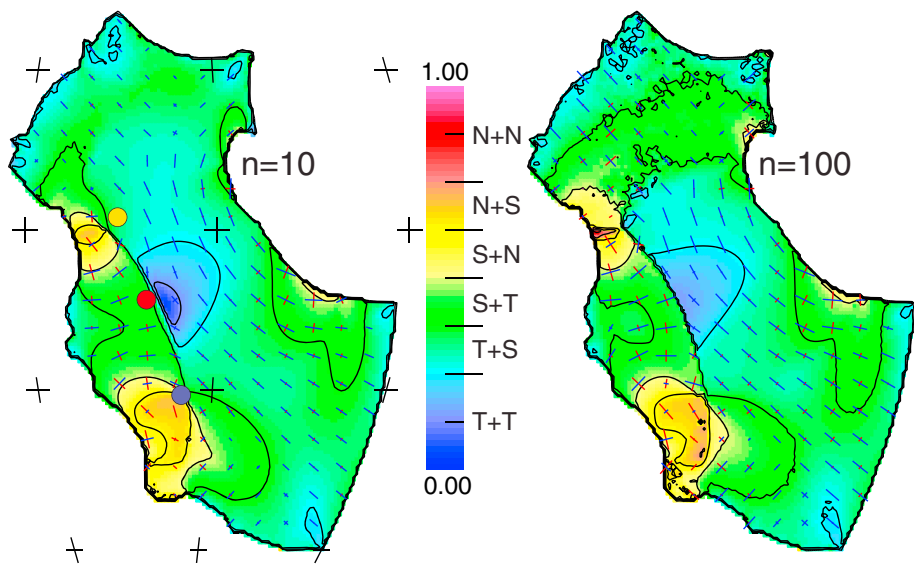


**Figure 6.** Contours of the parameter  $p$  (equation (9)) used to indicate the type of near-surface faulting implied by the computed viscous strain-rate field for (left)  $n = 10$  and (right)  $100$ . The contour interval of  $p = 0.125$  divides the faulting style into the four major types listed in the text. Values less than 0.25 indicate that strain is accommodated by thrust faulting in two orthogonal directions; values between 0.25 and 0.375 indicate a combination of thrust > strike-slip faulting; values between 0.375 and 0.5 indicate a combination of strike-slip > thrust faulting; values between 0.5 and 0.625 indicate a combination of strike-slip > normal faulting; values between 0.625 and 0.75 indicate a combination of normal > strike-slip faulting; and values greater than 0.75 indicate that strain is accommodated by normal faulting in two orthogonal directions. Superposed on each frame are arrows indicating the direction and relative magnitude of principal components of deviatoric stress (blue, compressive; red, tensile). The colored circles show the location of poles rotation used to set relative velocity on different boundary segments: India-Australia (red), India-Capricorn (yellow), and Capricorn-Australia (blue) [DeMets *et al.*, 2010].

represent the subduction rate of the plate; it represents an extensional displacement of the eastern part of the plate relative to a frame tied to the average velocity of the India and Australia Plates. The impact of this change to the boundary conditions is shown in Figure 7 for three different average (peak/2) displacement rate increments of  $3.3 \text{ mm a}^{-1}$ ,  $5 \text{ mm a}^{-1}$ , and  $10 \text{ mm a}^{-1}$ . We see that the region in which strike-slip faulting exceeds thrust faulting is expanded by increasing the amplitude, and by comparison with the observed extent of the region of strike-slip faulting (Figure 1), we infer that the required amplitude of the average downdip normal velocity is  $\approx 5 \text{ mm a}^{-1}$ ;  $10 \text{ mm a}^{-1}$  is too fast, resulting in normal faulting being predicted across a large area in the eastern part of the plate.

Changing the boundary condition on Sumatra also changes the north-south extent of deformation along  $81.5^\circ\text{E}$ . As the trench-normal velocity is increased, the north-south width of the deformation zone decreases (Figure 5, right), resulting in further incremental improvement in the fit to observations for the case of  $n = 30$ . For  $n = 10$  or  $100$ , as the trench-normal velocity is increased, the width of the deformation zone also decreases. With  $n = 10$  the decrease is not enough to give an acceptable fit to the observed width, but for  $n = 100$  the predicted width is still compatible with the observations.

#### 4. Discussion

In this paper we address the way in which oceanic lithosphere deforms by setting our calculations in a reference frame defined by the average plate motions of the India and Australia Plates [DeMets *et al.*, 2010]. We assume that the plate deforms according to a non-Newtonian viscosity law with depth-averaged properties, but we assume also that those properties do not vary with position in the composite plate. The localization of deformation that we predict is partly a consequence of the assumed geometry and boundary conditions, but the impact of the tapered boundary condition segments decays rapidly into the solution domain on a length scale comparable to their width. As Figure 4 shows, increasing the nonlinearity of the constitutive law causes increasingly localized strain. Deformation naturally localizes across the narrowest parts of the composite plate between boundary segments that define plate-like behavior. If deformation continues in

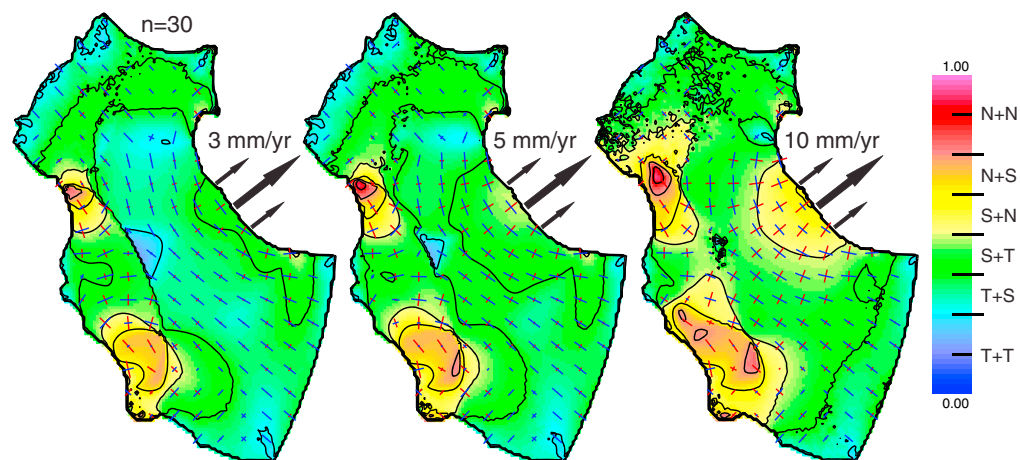


**Figure 7.** Maps of predicted double-couple mechanism types (as Figure 6) with  $n = 30$  and an additional velocity boundary condition imposed near the middle of the India-Australia diffuse plate boundary along the Sumatran Trench, representing the effect of an in-plane stress caused by slab pull. The angular velocity is tapered linearly to zero from a point in the middle of this edge segment (Table 1) to the nearest points on the India and Australia plate boundary segments. The average trench-normal velocity increments along this boundary (half the peak velocity) are (left) 3.3 mm/yr, (middle) 5 mm/yr, and (right) 10 mm/yr; the pole coordinates and angular velocity of the midpoint are given in Table 1. Superposed on each frame are arrows indicating the direction and relative magnitude of principal components of deviatoric stress (blue, compressive; red, tensile).

future geological time to the point where a clear boundary is established between the India and Australia Plates, the ridge of high strain-rates, evident in Figure 4 for greater values of  $n$ , indicates the location where a subduction system would most probably develop.

For  $n \geq \approx 30$  we obtain a distribution of deformation in the diffuse plate boundary that is a good approximation to that observed. In Figure 8 we compare intraplate earthquake locations, magnitudes, and mechanisms with fields determined for the model with  $n = 30$  and an incremental Sumatran Trench flux of  $5 \text{ mm a}^{-1}$ . Apart from a few significant earthquakes that occur near the continental margins of Australia and India, the earthquake activity is focused in those locations where the model strain-rates are highest (Figure 8a) and the combinations of earthquake mechanism (thrust, normal, or strike slip) are almost completely consistent with the predicted types of strain-rate tensor (Figure 8b): normal-type events are found only in those regions where  $p > 0.5$ , and thrust-type events are found only in those regions where  $p < 0.5$ ; strike-slip events occur when  $0.25 < p < 0.75$ , and they are dominant when  $0.375 < p < 0.625$ . Although many of the observed moment tensors have nondouble-couple components and have principal axes that are oblique to vertical/horizontal (see supporting information), Figure 8 simplifies this complexity by defining a mechanism type based on which principal axis is nearest to vertical:  $P$ ,  $T$ , or  $B$ .

The relatively high value of  $n$  ( $\geq \approx 30$ ) inferred from the width of the deformation zone shown in Figure 5 contrasts with other values of  $n$  estimated from analysis of continental deformation. For example, *England and Houseman [1986]*, *England and Molnar [1997]*, *Neil and Houseman [1997]*, and *Dayem et al. [2009]* variously estimated  $n$  values between about 3 and 10 for the deformation field of central Asia, though *Dayem et al. [2009]* concluded that some additional strain weakening mechanism was needed to explain the narrow width of deformation around the Altyn Tagh Fault system which separates Tibet from the Tarim Basin. They also noted that greater values of  $n$  could be explained by a change of deformation mechanism from power-law creep with  $n \approx 3$  to dislocation glide [Goetze, 1978; Evans and Goetze, 1979], with apparent  $n$  values up to  $\approx 25$ . The greater values of  $n$  in the oceanic lithosphere may be a consequence of the brittle-plastic transition occurring at greater depth than in the continents or an increased contribution of fracture, frictional sliding, or dislocation glide to the depth-averaged constitutive law.

The distribution of two key stress components ( $\sigma_{\theta\theta}$  and  $\sigma_{\theta\phi}$ ) within the plate for the same  $n = 30$  model is shown in Figure 9. A profile along the equator of these stress components shows a broad maximum in north-south compressive stress ( $\sigma_{\theta\theta}$ ) in the eastern equatorial part of the Indian Ocean where the India and Australia Plates converge (Figure 9b); west of about  $74^\circ\text{E}$ , the plate is extending in the north-south direction. The profile of compressive stress agrees well with that calculated by *Zatman et al. [2005]* for an

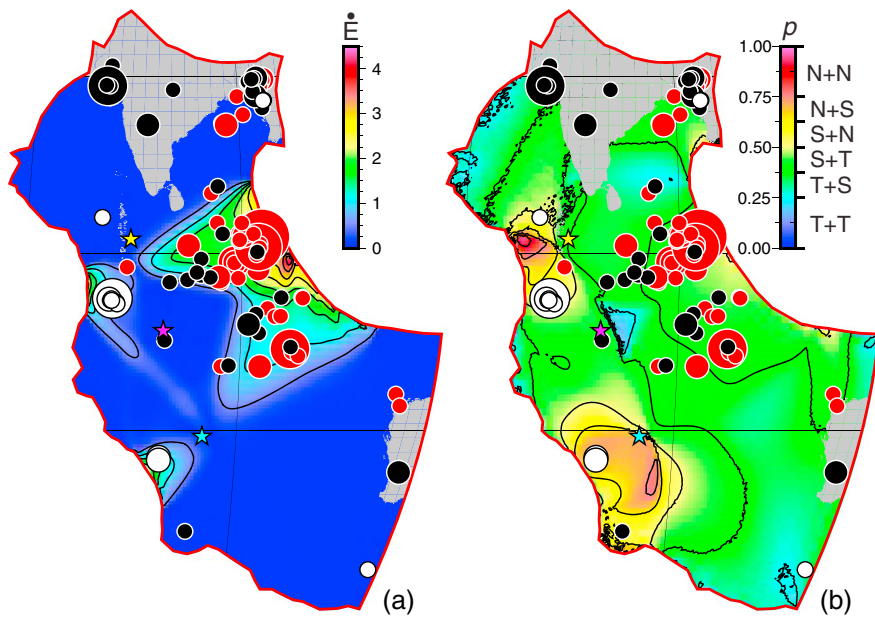


**Figure 8.** Maps of (a) second invariant of the strain rate and (b) double-couple mechanism types ( $p$ , as defined by equation (9)) for the solution with  $n = 30$  and trench velocity increment of  $5 \text{ mm a}^{-1}$  (as Figure 7, middle). Earthquake epicenters, magnitudes, and mechanism types (as Figure 1) are superposed, as are the locations of the poles of rotation.

idealized diffuse oceanic plate boundary with a pole of rotation lying inside the boundary. The change from north-south compression to north-south tension (relative to the reference lithostatic state) occurs on the neutral surface defined approximately by the line joining the two poles of rotation for India-Capricorn and Capricorn-Australia. Since a pole of rotation effectively corresponds to a  $180^\circ$  change in relative velocity on any line that crosses the pole, we expect that these poles effectively define the boundary between horizontal contraction to the east and horizontal extension to the west. That the three poles do not lie exactly on the neutral surface is likely explained by the influence of the short boundary segments on which we set the boundary rotation vector to change continuously from one value to the next.

The neutral surface also marks a change in sign of the in-plane shear stress ( $\sigma_{\theta\phi}$ , Figure 9c); the profile on the equatorial transect shows that the region north of the equator is pushed eastward on the eastern side of the plate and westward on the western side of the plate (relative to the region south of the equator). The steepness of the stress gradients across the neutral plane (Figure 9b) is enhanced by the strong nonlinearity of the constitutive law used in this calculation [Zatman *et al.*, 2005].

If we assume that the traction acting on the Himalayan boundary of the plate, (estimated by Molnar *et al.* [1993] as  $F \approx (8 \pm 2) \times 10^{12} \text{ N m}^{-1}$ ), is the principal nonlithostatic force acting on the plate boundary north of the equator, we can estimate the torque applied to the plate by this force as  $\mathbf{T} = F \mathbf{R} \mathbf{c}$ , where  $R$  is the radius of the Earth and  $\mathbf{c}$  is the chord that joins the two ends of the boundary segment (the two syntaxes at the ends of the Himalayan arc) [Gordon *et al.*, 1978]. Assuming that  $F$  acts in the direction normal to the chord, we obtain a torque of magnitude  $(1.1 \pm 0.2) \times 10^{26} \text{ N m}$  around an axis at  $165^\circ\text{E}, 14.9^\circ\text{S}$ .

In equilibrium a balancing torque must then apply on any surface that cuts the thin spherical sheet of nominal thickness  $L$ . We use the equatorial plane for simplicity and estimate for our preferred model ( $n=30$ , boundary velocity increment  $5 \text{ mm a}^{-1}$ ) the torque that the plate north of the equator applies to that south of the equator (and vice versa) by evaluating

$$\mathbf{T} = R^2 L \left( B \omega_0^{1/n} \right) \left( \int_{\partial\Omega} \sigma_{\theta\theta} \sin(\varphi_1 - \varphi) d\varphi, \int_{\partial\Omega} \sigma_{\theta\theta} \sin(\varphi_2 - \varphi) d\varphi, \int_{\partial\Omega} \sigma_{\theta\theta} d\varphi \right) \quad (10)$$

by numerical integration of the profiles shown in Figure 9b to obtain the components of torque in the directions defined by  $\varphi_1 = 0$ ,  $\varphi_2 = \pi/2$  ( $0^\circ\text{E}$  and  $90^\circ\text{E}$  on the equator), and  $90^\circ\text{N}$ . The factor,  $B \omega_0^{1/n}$ , for  $B$  the viscosity coefficient defined in (3) and  $\omega_0$  the rotation rate of the major plates with respect to the

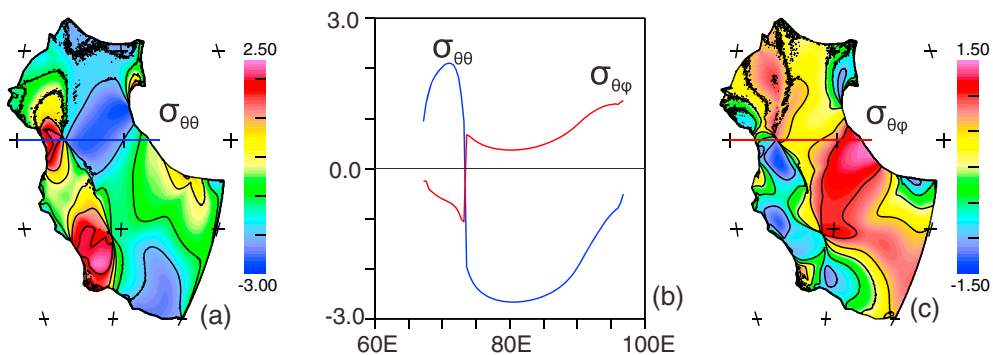


**Figure 9.** (a and c) Maps of the components of north-south normal stress (relative to the reference lithostatic state),  $\sigma_{\theta\theta}$  and shear stress,  $\sigma_{\theta\varphi}$ , for the calculation with  $n = 30$  and  $5 \text{ mm a}^{-1}$  trench velocity increment applied to the Sumatran boundary (as Figure 7, middle). (b) Profiles of  $\sigma_{\theta\theta}$  and  $\sigma_{\theta\varphi}$  along the equator between longitudes of  $60^\circ\text{E}$  and  $100^\circ\text{E}$ , as indicated by the lines on Figures 9a and 9c. Units of stress are dimensionless but may be scaled using the stress dimensionalization factor of  $40 \pm 8 \text{ MPa}$  (see text for discussion).

reference frame ( $0.1775^\circ/\text{Ma}$ , expressed in radians/s) is the scaling factor for dimensionless stress used in the calculations (Figures 9 and 10). The resulting torque has direction defined by an axis at  $177^\circ\text{E}, 18.1^\circ\text{N}$ . It differs in direction by  $35^\circ$  from the direction obtained using the estimated force on the Himalayan boundary. The difference in direction could result from us ignoring possible torques on the other boundary segments of the plate north of the equator (including basal stress), or from the Himalayan force acting obliquely to the chord that joins the syntaxes, or from errors in the assumed relative plate velocities. Nonetheless, the difference is small enough that we feel justified in equating the magnitudes of the two torque estimates. Thus, we constrain the value of  $B$  required to balance these torques:  $B \approx 1.3 \times 10^8 \text{ Pa s}^{1/30}$  and find the stress scaling factor required to dimensionalize stress components in Figures 9 and 10:  $\approx 40 \pm 8 \text{ MPa}$ .

A further consistency check on the magnitude of stress in these calculations is provided by examining the traction applied to the Sumatran boundary when we set an incremental velocity on that boundary segment. In Figure 10c we show that the least compressive principal stress directions near the Sumatra Trench are basically perpendicular to the plate boundary. Profiles of the magnitude of this principal stress component (Figure 10a) along a line that is close to and parallel to the Sumatra Trench (Figure 10b) show that for our calculation with  $n=30$  and trench flux increment of  $5 \text{ mm/yr}$ , the average normal force per unit length applied to this boundary is  $\approx (4 \pm 1) \times 10^{12} \text{ N m}^{-1}$ , comparable to  $\approx (3 \pm 1) \times 10^{12} \text{ N m}^{-1}$  inferred by Sandiford *et al.* [2005] from the distribution of earthquake mechanisms in the equatorial Indian Ocean.

Figure 10a also helps us to interpret our result that only a velocity increment near  $5 \text{ mm a}^{-1}$  predicts a distribution of focal mechanisms in agreement with that observed (Figure 7). With no velocity increment, the least compressive stress is negative along most of the trench. The increment of  $3.3 \text{ mm a}^{-1}$  increases the least compressive stress to near zero along most of the boundary, while only the increments of  $5 \text{ mm a}^{-1}$  and  $10 \text{ mm a}^{-1}$  predicted a positive trench-normal least compressive stress (the latter of which is too great as it predicts normal faulting earthquakes across a large area (Figure 7)).

The principal stress directions and magnitudes shown in Figure 10 are generally consistent with earthquake principal stress directions (supporting information) and reflect the way in which counteracting torques on the India and Australia parts of the composite plate are balanced. The approximately north-south oriented compressive stress in the Central Indian Basin reaches an amplitude of  $\approx 110 \pm 20 \text{ MPa}$  (depth averaged, corresponding to a force per unit length of  $\approx (11 \pm 2) \times 10^{12} \text{ N m}^{-1}$ ). Our estimate is at the high end of the range  $(5-11) \times 10^{12} \text{ N m}^{-1}$  determined using a plastic instability model [Martinod and Molnar, 1995], similar to the lower bound of  $(11 \pm 3) \times 10^{12} \text{ N m}^{-1}$  inferred by Gordon [2000] from the model of Martinod and Molnar [1995], more than twice as large as the maximum depth-averaged stress,  $\approx 40 \text{ MPa}$ , in the Central Indian Basin estimated by Sandiford *et al.* [2005], but less than the maximum compressive (deviatoric) stress in the region, 200 to 300 MPa, indicated in Figure 1 of Cloetingh and Wortel [1985].

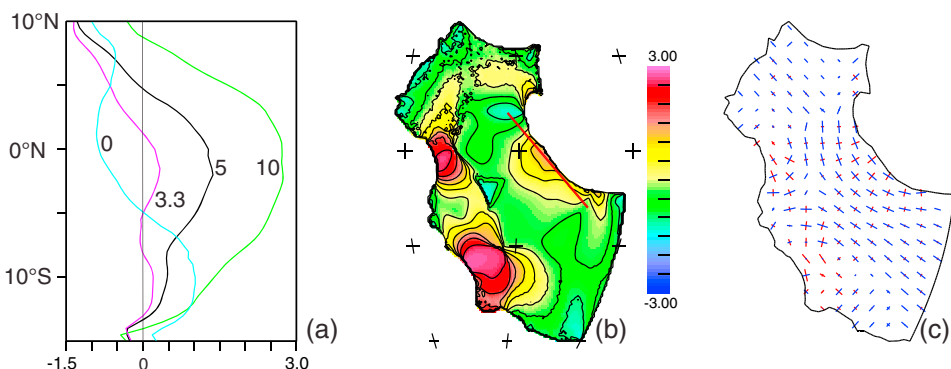


**Figure 10.** (a) Profiles of the least compressive principal stress component (relative to the reference lithostatic state) plotted along a line joining endpoints at  $(87^\circ\text{E}, 10^\circ\text{N})$  and  $(109^\circ\text{E}, 15^\circ\text{S})$  for the  $n=30$  solutions with Sumatran Trench velocity increments respectively of 0, 3.3, 5, and  $10 \text{ mm a}^{-1}$ . (b) The profile location is indicated by a red line superposed on the contour plot of that stress component. (c) Directions and relative magnitudes of the two principal deviatoric stress components; the red arm of each cross indicates tension and the blue arm indicates compression. Dimensionless stress units may be scaled by the factor  $40 \pm 8$  MPa. Figures 10b and 10c are for the solution with a trench-normal velocity increment of  $5 \text{ mm a}^{-1}$ . The black crosses in Figure 10b are coordinate marks at intervals of  $25^\circ$  in latitude and  $30^\circ$  in longitude, as other maps.

#### 4.1. Caveats

The thin viscous sheet model with constant viscous coefficient and  $n \geq \approx 30$  can explain most of the observations of recent deformation in the Central Indian Ocean. Although previous studies [e.g., *England and Houseman, 1986; England and Molnar, 1991, 1997; Neil and Houseman, 1997*] found that the power-law exponent for the depth-averaged constitutive law for the continents may be as low as 3, the relative absence of deformation within the Australian and Indian continents (Figure 1) does not allow any useful constraint on a contrast in effective  $n$  value from continent to ocean. Moreover, the application of plate-like boundary velocities on the perimeter (Figure 3, left), in conjunction with the assumed uniform rheological coefficient, acts to produce a set of boundary tractions that distribute the load around a plate boundary. In these circumstances the boundary tractions driving the relative motion of India within the model predict NW-SE principal stress axes across most of India, approximately perpendicular to its NW boundary segment. In reality, however, the collision of India with Eurasia along the Himalayan front and the development of the Tibetan Plateau have resulted in a distribution of boundary tractions that is actually dominated by south to southwest directed traction acting on the Himalayan front [e.g., *Zoback et al., 1989; Heidbach et al., 2008; Warners-Ruckstuhl et al., 2010*] and transmitted across the Indian subcontinent.

The north-south strain-rate profiles for  $n=10, 30$ , and  $100$  (Figure 5) are close to symmetric about the peak strain-rate at about  $2^\circ\text{N}$  and contrast with the apparent asymmetry of the observed deformation profile, which increases abruptly just south of the equator, peaks at about  $1^\circ\text{S}$ , and decreases more gradually southward [*Chamot-Rooke et al., 1993; Gordon, 2000*]. These differences might be explained by lithospheric strength decreasing southward where the lithosphere is younger. In reality, of course, the resistance to deformation is expected to vary with position in the plate, increasing with age, as the plate cools and the thickness of the faulted upper layer increases. Maps of the age variation of the Indian Ocean [*Patriat and Segoufin, 1988; Müller et al., 2008*] show that the ocean floor is typically 90 to 100 Ma old in the eastern part of the Central Indian Ocean, with the principal exception of a ridge of younger ( $\approx 50$  Ma) crust that runs NNE-SSW through the Wharton Basin. To the west and southwest the age decreases systematically to zero at the mid-ocean ridge. We expect that the major features of the stress distribution described here will be robust to the variation of viscous resistance due to plate age, but localization of strain-rates may be further enhanced. Further calculations with a spatially variable viscosity coefficient are needed to test this expectation.

#### 4.2. Simplicity

In the end, we emphasize that the power of our analysis lies in its simplicity. In the set of models described in this paper we adjust merely two parameters, the power-law exponent,  $n$ , and the magnitude  $v$  of incremental

trench-normal velocity of lithosphere toward the Sumatra Trench. Varying the first parameter,  $n$ , gives rise to large variations in the distribution of strain-rate in the model domain. Only values of  $n \geq 30$  give rise to strain that was localized enough to give an acceptable fit to the observed north-south extent of deformation in the Central Indian Basin. Varying the second parameter,  $v$ , gives rise to large variations in the predicted distribution of earthquake focal mechanisms. Only if  $v$  is  $\approx 5 \text{ mm a}^{-1}$  ( $3.3 \text{ mm a}^{-1} < v < 10 \text{ mm a}^{-1}$ ) do we obtain an acceptable fit to the distribution of earthquake mechanisms. With only two adjustable parameters we are able to construct models that provide an excellent fit to both the distribution of the observed strain-rates and the distribution of the style of faulting. More importantly, we show that models with a power-law exponent  $< 30$  predict an unacceptably wide north-south extent of the deformation and that an incremental velocity along the Sumatra Trench much different from  $\approx 5 \text{ mm a}^{-1}$  predicts focal mechanisms that differ unacceptably from those observed.

## 5. Conclusions

1. The predicted distribution of strain-rate varies strongly with power-law exponent with the deforming zones becoming narrower and the edges of the deforming zones becoming more sharply defined, as power-law exponent increases. Thus, the observed distribution of strain can be used to place limits on what value of the power-law exponent is appropriate. The deformation is too diffusely distributed for power-law exponents of 1, 3, and 10 but is approximately correct for a power-law exponent  $\geq 30$ .
2. The thin viscous sheet model can be used to predict strain-state domains within the India-Capricorn-Australia diffuse deformation zone in which different combinations of earthquake focal mechanisms should occur. Without a velocity increment of lithosphere into the Sumatran Trench (representing a pull from the subducted slab), the predictions do not match the observations. An average velocity increment of  $3.3 \text{ mm a}^{-1}$  is too small to match observations, one of  $10 \text{ mm a}^{-1}$  is too large, but one of  $5 \text{ mm a}^{-1}$  is about right. The average force per unit length acting on this plate boundary is estimated at  $\approx (4 \pm 1) \times 10^{12} \text{ N m}^{-1}$ .
3. The introduction of a velocity increment at the Sumatran Trench modestly affects the distribution of strain in the diffuse plate boundary. In particular, the equatorial zone of lithospheric thickening becomes a little narrower and in the case of  $n = 30$  more closely matches the observed north-south width of this zone as indicated on seismic profiles and satellite-derived gravity for the Central Indian Basin.

## Acknowledgments

This work was partly supported by NSF grant OCE-1131638. G.H. has been supported by the Natural Environment Research Council through funding of the National Centre for Earth Observation (COMET+). We thank Lynn Evans for numerous contributions to the development and maintenance of the program *basil* [Houseman et al., 2008] used for the thin-sheet calculations. We thank Philip England and Wouter Schellart for their constructive reviews of an earlier version of this manuscript. The sources of gravity and seismic data used in this study are described in the supporting information. GMT [Wessel et al., 2013] has been used to draft some of the figures.

## References

- Atwater, T. (1970), Implications of plate tectonics for the Cenozoic tectonic evolution of western North America, *Bull. Geol. Soc. Am.*, 81, 3513–3536.
- Ball, M. M., and C. G. A. Harrison (1970), Crustal plates in the central Atlantic, *Science*, 167, 1128–1129.
- Bird, P. (2003), An updated digital model of plate boundaries, *Geochem. Geophys. Geosyst.*, 4(3), 1027, doi:10.1029/2001GC000252.
- Bird, P., and K. Piper (1980), Plane-stress finite-element models of tectonic flow in Southern California, *Phys. Earth Planet. Inter.*, 21, 158–175.
- Bull, J. M. (1990), Structural style of intraplate deformation, Central Indian Ocean Basin: Evidence for the role of fracture zones, *Tectonophysics*, 184, 213–228.
- Bull, J. M., and R. A. Scrutton (1990), Fault reactivation in the Central Indian Ocean and the rheology of oceanic lithosphere, *Nature*, 344, 855–858.
- Burbidge, D. R. (2004), Thin plate neotectonic models of the Australian Plate, *J. Geophys. Res.*, 109, B10405, doi:10.1029/2004JB003156.
- Cande, S. C., and J. M. Stock (2004), Pacific-Antarctic-Australia motion and the formation of the Macquarie Plate, *Geophys. J. Int.*, 157, 399–414, doi:10.1111/j.1365-246X.2004.02224.x.
- Chamot-Rooke, N., F. Jfestin, B. De Voogd, and Phedre Working Group (1993), Intraplate shortening in the Central Indian Ocean determined from a 2100 km long north-south deep seismic reflection profile, *Geology*, 21, 1043–1045.
- Chu, D., and R. G. Gordon (1999), Evidence for motion between Nubia and Somalia along the Southwest Indian Ridge, *Nature*, 398, 64–67.
- Cloetingh, S., and R. Wortel (1985), Regional stress field of the Indian Plate, *Geophys. Res. Lett.*, 12, 77–80, doi:10.1029/GL012i002p00077.
- Coblenz, D. S., Zhou, R. R. Hillis, R. M. Richardson, and M. Sandiford (1998), Topography, boundary forces, and the Indo-Australian intraplate stress field, *J. Geophys. Res.*, 103, 919–931, doi:10.1029/97JB02381.
- Curry, J. R., and D. G. Moore (1971), Growth of the Bengal deep-sea fan and denudation in the Himalayas, *Bull. Geol. Soc. Am.*, 82, 563–572.
- Dayem, K. E., G. A. Houseman, and P. Molnar (2009), Localization of shear along a lithospheric strength discontinuity: Application of a continuous deformation model to the boundary between Tibet and the Tarim Basin, *Tectonics*, 28, TC3002, doi:10.1029/2008TC002264.
- Delescluse, M., and N. Chamot-Rooke (2007), Instantaneous deformation and kinematics of the India-Australia Plate, *Geophys. J. Int.*, 168, 818–842, doi:10.1111/j.1365-246X.2006.03181.x.
- Delescluse, M., L. Montési, and N. Chamot-Rooke (2008), Fault reactivation and selective abandonment in the oceanic lithosphere, *Geophys. Res. Lett.*, 35, L16312, doi:10.1029/2008GL035066.
- DeMets, C., R. G. Gordon, D. F. Argus, and S. Stein (1990), Current plate motions, *Geophys. J. Int.*, 101, 425–478.
- DeMets, C., R. G. Gordon, and J.-Y. Royer (2005), Motion between the Indian, Capricorn, and Somalian Plates since 20 Ma: Implications for the timing and magnitude of distributed deformation in the equatorial Indian Ocean, *Geophys. J. Int.*, 161, 445–468.
- DeMets, D. C., R. G. Gordon, and D. F. Argus (2010), Geologically current plate motions, *Geophys. J. Int.*, 181, 1–80, doi:10.1111/j.1365-246X.2009.04491.x.

- Eittreim, S. L., and J. Ewing (1972), Midplate tectonics in the Indian Ocean, *J. Geophys. Res.*, 77, 6413–6421, doi:10.1029/JB077i032p06413.
- England, P., and G. Houseman (1986), Finite strain calculations of continental deformation: 2. Comparison with the India-Asia collision zone, *J. Geophys. Res.*, 91, 3664–3676, doi:10.1029/JB091iB03p03664.
- England, P., and P. Molnar (1991), Inferences of deviatoric stress in actively deforming belts from simple physical models, *Philos. Trans. R. Soc. London A*, 337, 151–164.
- England, P., and P. Molnar (1997), Deformation of Asia: From kinematics to dynamics, *Science*, 278, 647–650, doi:10.1126/science.278.5338.647.
- England, P. C., and D. P. McKenzie (1982), A thin viscous sheet model for continental deformation, *Geophys. J. R. Astron. Soc.*, 70, 295–321.
- Evans, B., and C. Goetze (1979), The temperature variation of hardness of olivine and its implication for polycrystalline yield stress, *J. Geophys. Res.*, 84, 5505–5524, doi:10.1029/JB084iB10p05505.
- Gerbault, M. (2000), At what stress level is the Central Indian Ocean lithosphere buckling?, *Earth Planet. Sci. Lett.*, 178, 165–181.
- Gerbault, M., E. B. Burov, A. N. B. Poliakov, and M. Daignières (1999), Do faults trigger folding in the lithosphere?, *Geophys. Res. Lett.*, 26, 271–274, doi:10.1029/1998GL900293.
- Goetze, C. (1978), The mechanisms of creep in olivine, *Philos. Trans. R. Soc. London A*, 288, 99–119.
- Gordon, R. G. (1998), The plate tectonic approximation: Plate non-rigidity, diffuse plate boundaries, and global plate reconstructions, *Annu. Rev. Earth Planet. Sci.*, 26, 615–642.
- Gordon, R. G. (2000), Diffuse oceanic plate boundaries: strain-rates, vertically averaged rheology and comparisons with narrow plate boundaries and stable plate interiors, in *The History and Dynamics of Global Plate Motions*, *Geophys. Monogr.*, vol. 121, edited by M. A. Richards, R. G. Gordon, and R. D. van der Hilst, pp. 143–159, AGU, Washington, D. C.
- Gordon, R. G., and S. Stein (1992), Global tectonics and space geodesy, *Science*, 256, 333–342.
- Gordon, R. G., A. Cox, and C. E. Harter (1978), Absolute motion of an individual plate estimated from its ridge and trench boundaries, *Nature*, 274(5673), 752–755.
- Gordon, R. G., C. DeMets, and D. F. Argus (1990), Kinematic constraints on distributed lithospheric deformation in the equatorial Indian Ocean from present motion between the Australian and Indian Plates, *Tectonics*, 9, 409–422, doi:10.1029/TC009i003p00409.
- Gordon, R. G., D. F. Argus, and J.-Y. Royer (2008), Space geodetic test of kinematic models for the Indo-Australian composite plate, *Geology*, 36, 827–830.
- Heidbach, O., M. Tingay, A. Barth, J. Reinecker, D. Kurfess, and B. Mueller (2008), World stress map, Commission for the Geological Map of the World. [Available at <http://www.world-stress-map.org/>.]
- Houseman, G., and P. England (1986), Finite strain calculations of continental deformation: 1. Methods and general results for convergent zones, *J. Geophys. Res.*, 91, 3651–3663, doi:10.1029/JB091iB03p03651.
- Houseman, G. A., and P. C. England (1993), Crustal thickening versus lateral expulsion in the Indian-Asian continental collision, *J. Geophys. Res.*, 98, 12,233–12,249, doi:10.1029/93JB00443.
- Houseman, G. A., T. D. Barr, and L. A. Evans (2008), Basil: Stress and deformation in a viscous material, in *Microdynamics Simulation, Lect. Notes in Earth Sci.*, vol. 106, edited by P. D. Bons, D. Koehn, and M. W. Jessell, chap. 3.8, pp. 77–85, Springer, Berlin.
- Isacks, B., J. Oliver, and L. R. Sykes (1968), Seismology and the new global tectonics, *J. Geophys. Res.*, 73, 5855–5899, doi:10.1029/JB073i018p05855.
- Jestin, F., P. Huchon, and J. M. Gaulier (1994), The Somalia Plate and the East African Rift System: Present-day kinematics, *Geophys. J. Int.*, 116, 637–654.
- Kohlstedt, D. L., B. Evans, and S. J. Mackwell (1995), Strength of the lithosphere: Constraints imposed by laboratory experiments, *J. Geophys. Res.*, 100, 17,587–17,602, doi:10.1029/95JB01460.
- Kreemer, C., W. E. Holt, and A. J. Haines (2003), An integrated global model of present-day plate motions and plate boundary deformation, *Geophys. J. Int.*, 154, 8–34, doi:10.1046/j.1365-246X.2003.01917.x.
- Kumar, R. V., and R. G. Gordon (2009), Horizontal thermal contraction of oceanic lithosphere: The ultimate limit to the rigid plate approximation, *J. Geophys. Res.*, 114, B01403, doi:10.1029/2007JB005473.
- Kusznir, N. J., and M. H. P. Bott (1977), Stress concentration in the upper lithosphere caused by underlying visco-elastic creep, *Tectonophysics*, 43, 247–256.
- Le Pichon, X. (1983), Land-locked oceanic basins and continental collision, in *Mountain Building Processes*, edited by K. J. Hsu, pp. 201–212, Academic Press, London.
- Martinod, J., and P. Molnar (1995), Lithospheric folding in the Indian Ocean and the rheology of the oceanic plate, *Bull. Soc. Géol. Fr.*, 166, 813–821.
- Mei, S., A. Suzuki, D. L. Kohlstedt, N. A. Dixon, and W. B. Durham (2010), Experimental constraints on the strength of the lithospheric mantle, *J. Geophys. Res.*, 115, B08204, doi:10.1029/2009JB006873.
- Minster, J. B., and T. H. Jordan (1978), Present-day plate motions, *J. Geophys. Res.*, 83, 5331–5354, doi:10.1029/JB083iB11p05331.
- Molnar, P., P. England, and J. Martinod (1993), Mantle dynamics, uplift of the Tibetan Plateau, and the Indian Monsoon, *Rev. Geophys.*, 31, 357–396.
- Montesi, L. G. J., and M. T. Zuber (2003), Spacing of faults at the scale of the lithosphere and localization instability: 2. Application to the Central Indian Basin, *J. Geophys. Res.*, 108(B2), 2111, doi:10.1029/2002JB001924.
- Müller, R. D., M. Sdrolias, C. Gaina, and W. R. Roest (2008), Age, spreading rates, and spreading asymmetry of the world's ocean crust, *Geochem. Geophys. Geosyst.*, 9, Q04006, doi:10.1029/2007GC001743.
- Neil, E. A., and G. A. Houseman (1997), Geodynamics of the Tarim Basin and the Tian Shan in central Asia, *Tectonics*, 16, 571–584, doi:10.1029/97TC01413.
- Patriat, P., and J. Segoufin (1988), Reconstruction of the Central Indian Ocean, *Tectonophysics*, 155, 211–234.
- Raterron, P., Y. Wu, D. J. Weidner, and J. Chen (2004), Low-temperature olivine rheology at high pressure, *Phys. Earth Planet. Inter.*, 145, 149–159.
- Roberts, E. A., and G. A. Houseman (2001), Geodynamics of central Australia during the intraplate Alice Springs Orogeny: Thin viscous sheet models, in *Continental Reactivation and Reworking*, edited by J. A. Miller et al., *Geol. Soc. London Spec. Publ.*, 184, 139–164, doi:10.1144/GSL.SP.2001.184.01.08.
- Royer, J.-Y., and R. G. Gordon (1997), The motion and boundary between the Capricorn and Australian Plates, *Science*, 277, 1268–1274.
- Sandiford, M., D. Coblenz, and W. P. Schellart (2005), Evaluating slab-plate coupling in the Indo-Australian Plate, *Geology*, 33, 113–116, doi:10.1130/G20898.1.
- Sandwell, D. T., R. D. Muller, W. H. F. Smith, E. Garcia, and R. Francis (2014), New global marine gravity model from Cryosat-2 and Jason-1 reveals buried tectonic structure, *Science*, 346, 65–67, doi:10.1126/science.1258213.
- Shewchuk, J. R. (2002), Delaunay refinement algorithms for triangular mesh generation, *Comput. Geom. Theory Appl.*, 22(1–3), 21–74.

- Sonder, L. J., and P. C. England (1986), Vertical averages of rheology of the continental lithosphere: Relation to thin sheet parameters, *Earth Planet. Sci. Lett.*, 77, 81–90.
- Stein, S., and E. O. Okal (1978), Seismicity and tectonics of the Ninetyeast Ridge area: Evidence for internal deformation of the Indian plate, *J. Geophys. Res.*, 83, 2233–2246, doi:10.1029/JB083iB05p02233.
- Tapponnier, P., and P. Molnar (1977), Active faulting and tectonics in China, *J. Geophys. Res.*, 82, 2905–2930, doi:10.1029/JB082i020p02905.
- Tinson, M. J., W. E. Holt, and A. J. Haines (1995), Velocity gradients in the northern Indian Ocean inferred from earthquake moment tensors and relative plate velocities, *J. Geophys. Res.*, 100, 24,315–24,329, doi:10.1029/95JB02910.
- Vilotte, J. P., M. Daignières, and R. Madariaga (1982), Numerical modeling of intraplate deformation: Simple mechanical models of continental collision, *J. Geophys. Res.*, 87, 10,709–10,728, doi:10.1029/JB087iB13p10709.
- Warners-Ruckstuhl, K., P. T. Meijer, R. Govers, and M. J. R. Wortel (2010), A lithosphere-dynamics constraint on mantle flow: Analysis of the Eurasian plate, *Geophys. Res. Lett.*, 37, L18308, doi:10.1029/2010GL044431.
- Weissel, J., R. Anderson, and C. Geller (1980), Deformation of the Indo-Australian Plate, *Nature*, 287, 284–291.
- Wessel, P., W. H. F. Smith, R. Scharroo, J. F. Luis, and F. Wobbe (2013), Generic Mapping Tools: Improved version released, *Eos Trans. AGU*, 94, 409–410, doi:10.1002/2013EO450001.
- Wiens, D. A., et al. (1985), A diffuse plate boundary model for Indian Ocean tectonics, *Geophys. Res. Lett.*, 12, 429–432, doi:10.1029/GL012i007p00429.
- Zatman, S., R. G. Gordon, and M. A. Richards (2001), Analytic models for the dynamics of diffuse oceanic plate boundaries, *Geophys. J. Int.*, 145, 145–156.
- Zatman, S., R. G. Gordon, and K. Mutnuri (2005), Dynamics of diffuse oceanic plate boundaries: Insensitivity to rheology, *Geophys. J. Int.*, 162, 239–248.
- Zoback, M. L., et al. (1989), Global patterns of tectonic stress, *Nature*, 341, 291–298.
- Zuber, M. T., and E. M. Parmentier (1996), Finite amplitude folding of a continuously viscosity-stratified lithosphere, *J. Geophys. Res.*, 101, 5489–5498, doi:10.1029/95JB02514.